Macro-Mesoscale In-Pile Thermal-Mechanical Behavior Simulation of a UMo/Zr Monolithic Fuel Plate

Xiangzhe Kong[1], Xiaobin Jian[1], Feng Yan[1], Wenjie Li[2], Zixuan Guo[2], Chuan Lu[2], Shurong Ding[1]* and Yuanming Li[2]

[1]Institute of Mechanics and Computational Engineering, Department of Aeronautics and Astronautics, Fudan University, Shanghai, China, [2]Science and Technology on Reactor System Design Technology Laboratory, Nuclear Power Institute of China, Chengdu, China

UMo/Zr monolithic fuel plates have a promising application prospect in high flux research reactors. To prolong the service life and achieve safety design, the in-pile macro-mesoscale thermal-mechanical behavior of the fuel plate needs further simulation research. In this study, for the fuel meat, the theoretical models of the equivalent fission gas bubble volume fraction, the gas-bubble inner pressure and the maximum skeleton stress are developed, with the effects of bubble distribution pattern involved. The application into the simulation of the in-pile macro-mesoscale thermal-mechanical behavior of the UMo/Zr monolithic fuel plate indicates that the maximum skeleton stress of the fuel meat basically rises with the burn-up, and may reach four times of the macroscale first principal stress of the fuel meat. The distribution patterns of the gas bubbles in the fuel meat might have a distinct influence on the maximum skeleton stress, and the most conservative results of the simple cubic arrangement can be used for the failure prediction of the fuel meat.

Keywords: UMo/Zr, irradiation-thermal-mechanical behavior, gas-bubble volume fraction, gasbubble inner pressure, skeleton stress

INTRODUCTION

UMo alloys are the main fuel candidates in the development of RERTR (Reduced Enrichment for Research and Test Reactors) program due to advantages of high uranium density and steady irradiation performance (Snelgrove et al., 1997; Burkes et al., 2015). Compared to UMo dispersion fuel elements, UMo monolithic fuel elements possess a higher uranium density (Gan et al., 2017). Aluminum alloy is the first choice for the cladding material in the research-test-reactor used fuel elements, because of its high thermal conductivity, low price and low density (Pasqualini et al., 2016). However, the fission fragment bombardment of the interface between aluminum alloy cladding and UMo fuel meat takes place under the in-pile irradiation environments, which will weaken the strength of UMo/Al interface resulting in the failure of fuel element and the reduction of the service life of fuel element (Pasqualini et al., 2016). The irradiation experiment results (Pasqualini et al., 2016) indicated that the interfacial performance of UMo/Al monolithic fuel element could be obviously improved by adding a Zr diffusion barrier layer between UMo fuel meat and Al alloy cladding or using Zr alloy cladding. Compared to Al alloy, the mechanical properties of Zr Alloy at
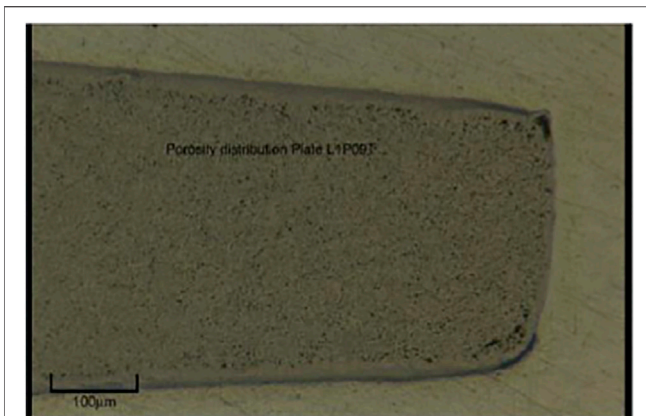
FIGURE 1 | Post irradiation section of a UMo fuel meat (Rice, 2010)

FIGURE 2 | The recrystallization region and the unrecrystallization region.

high temperatures are more similar to UMo alloy (Pasqualini et al., 2016). Hence, UMo/Zr monolithic fuel elements have a good application prospect in the future high flux research reactor (Gonzalez et al., 2015; Zhao et al., 2015) and advanced pressurized water reactor, because of its low neutron absorption cross section, good mechanical properties and corrosion resistance. The researches on the fabrication process and irradiation-induced behavior for UMo/Zr monolithic fuel elements have been implemented (Kong et al., 2016; Pasqualini et al., 2016).

For the safety operation of the reactor, the UMo/Zr monolithic fuel plates should be ensured with enough strength, stiffness and in-pile stability, which are closely related to the irradiation behaviors of UMo fuel meat and Zr alloy cladding together with their intense mechanical interactions. The UMo/Zr monolithic fuel plate experiences complex thermal-mechanical behavior under neutron irradiation. Firstly, the heat generation of the UMo fuel meat will cause non-uniform temperature field in the fuel plate, which causes certain temperature gradients and thermal stress in the fuel element (Yan et al., 2019a). In addition, the solid and gas fission products lead to the volume growth of the UMo fuel meat (Kong et al., 2018). The fission gas swelling is dependent on the nucleation and growth of fission gas bubbles and affected by stress state, fission rate, temperature and recrystallization effect (Kong et al., 2016; Yan et al., 2019a; Kong et al., 2018), etc. As shown in **Figure 1**, the fission gas bubbles make the UMo fuel meat a porous structure, which will continue to evolve with the development of burn-up (Meyer et al., 2014). The external stresses will be balanced by the ones in the solid part of the fuel meat, called as the fuel skeleton, and the pore pressures. Large gas bubbles or pores are observed in the fuel meat near the interface between fuel meat and the Zr barrier (Jue et al., 2018). The porosity may reach 20% (Salvato et al., 2018). The porosity and bubble pressure will affect the thermal-mechanical properties (Liu and Chen, 2015; Liu et al., 2016), and affect the stresses of the UMo skeleton structure by reducing the effective load-bearing cross-section. As for Zr alloy cladding, the impact due to fast neutrons results in the voids and interstitial atoms inside the material, and finally influences the thermal-mechanical
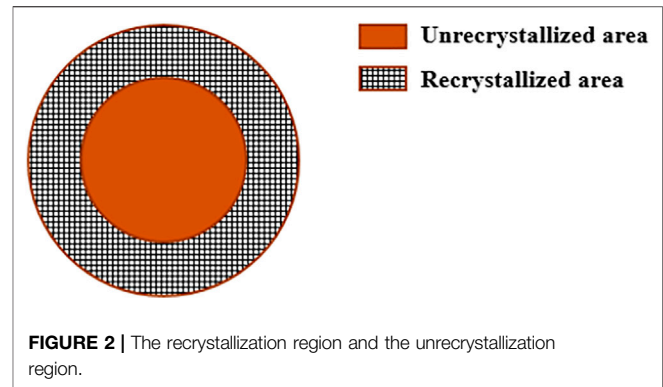
properties of material, causing the irradiation damage effects, such as irradiation hardening, irradiation embrittlement, irradiation creep and irradiation growth (Rodriguez et al., 1984; Holt and Causey, 2004; Rowcliffe et al., 2009). A study should be performed to investigate the differences in the in-pile thermal-mechanical behavior of UMo/Zr monolithic fuel elements and UMo/Al monolithic fuel elements (Kim and Hofman, 2011).

Irradiation tests are the direct means to study the in-pile thermal-mechanical behavior of UMo/Zr monolithic fuel element (Perez et al., 2007; Perez et al., 2012). Simultaneously, numerical simulation has become an important and effective mean to study the distribution and evolution laws of in-pile behavior. A number of numerical researches appear on the in-pile behavior of UMo/Al monolithic fuel plate (Miller et al., 2010; Kim and Hofman, 2011; Miller and Ozaltun, 2012; Kong et al., 2018). However, the related numerical simulation researches for UMo/Zr monolithic fuel plates are limited (Zhao et al., 2015). The mesoscale-structure, pore pressure and the macroscale thermal-mechanical behavior should be comprehensively correlated.

In this research, the model of the maximum skeleton stress for the fuel meat is further developed with the effects of bubble distribution pattern considered, which are introduced into the simulation of the thermal-mechanical behavior of the UMo/Zr monolithic fuel plate. The obtained macro-mesoscale mechanical field variables are analyzed.

THE THEORETICAL MODELS FOR THE MACRO-MESOSCALE BEHAVIOR OF U-MO FUEL MEAT

Gas Atom Number in the Gas Bubbles

According to Booth model (Booth, 1957; Cui et al., 2015), the origin grain of the UMo fuel meat could be treated as two parts, including the recrystallization region and the unrecrystallization region, once the recrystallization of fuel meat starts, as shown in **Figure 2**.

The fission gas atoms in the unrecrystallization region satisfy (Cui et al., 2015):

$$c_g + c_b n_b + 3N/2r_{gr} = Y\dot{f}t \qquad (1)$$

where c_g means the concentration of the gas atoms dissolved in the crystal lattice in atom/m3; n_b and c_b are respectively the average gas atom number in one intragranular bubble and the average concentration of the intragranular gas bubbles in 1/m³; r_{gr} in m is the equivalent grain radius of the unrecrystallization region; N in 1/m² represents the surface concentration of gas atoms on the grain boundary; Y means the gas atom number produced per fission; $\dot{f}$ is the fission rate in fissions/(m3·s) and t is the time in s. The average fission-gas concentration in the bubbles of the unrecrystallization region is:

$$\Psi = Y\dot{f}t - c_g \qquad (2)$$

The total number of fission gas atoms in the bubbles of the unrecrystallization region is:

$$\Sigma\Psi = \Psi \cdot \frac{4}{3}\pi r_{gr}^3 = \Psi \cdot \frac{4}{3}\pi r_{gr0}^3 \cdot (1 - v_r) \qquad (3)$$

in which r_{gr0} is the original grain radius in m, and v_r is the volume fraction of the recrystallized region.

For the recrystallization region, almost all the fission gas atoms will transfer to the intergranular bubbles (Rest, 2005). For each grain, the gas atom number in the intergranular bubbles is:

$$\Phi = \frac{1}{2}N_{bx}C_{bx} \cdot 4\pi r_{grx}^2 \qquad (4)$$

N_{bx} and C_{bx} are respectively the average gas-atom number in one intergranular bubble and the average surface concentration of the intergranular bubbles in 1/m²; r_{grx} in m is the grain radius in the recrystallization region. The total number of gas atoms in all the intergranular bubbles of the recrystallization region is:

$$\Sigma\Phi = \Phi v_r \cdot \frac{\frac{4}{3}\pi r_{gr0}^3}{\frac{4}{3}\pi r_{grx}^3} = \frac{3}{2}N_{bx}C_{bx}v_r \cdot \frac{\frac{4}{3}\pi r_{gr0}^3}{r_{grx}} \qquad (5)$$

The number of gas atoms in the gas bubbles per unit volume of the original fuel meat is:

$$n_\Sigma = \frac{\Sigma\Psi + \Sigma\Phi}{\frac{4}{3}\pi r_{gr0}^3} = \left(Y\dot{f}t - c_g\right) \cdot (1 - v_r) + \frac{3N_{bx}C_{bx}v_r}{2r_{grx}} \qquad (6)$$

The parameters including $N, c_g, n_b, c_b, N_{bx}, C_{bx}$ and v_r could be found in the reference (Cui et al., 2015). After completing the recrystallization process, $n_\Sigma = \frac{3N_{bx}C_{bx}}{2r_{grx}}$.

In the unrecrystallization area, most of the fission-gas atoms are in the intragranular bubbles or in solution of the fuel matrix. These bubbles are quite small, and the internal pressure will be balanced by the surface tension to affect the stresses of the fuel skeleton slightly. When considering only the gas atoms in the intergranular bubbles, **Eq. 2** should be re-described as:

$$\Psi_2 = Y\dot{f}t - c_g - c_b n_b \qquad (7)$$

Finally, the number of gas atoms in the intergranular gas bubbles per unit volume of the original fuel meat is given as:

$$n_{\Sigma 2} = \frac{\Sigma\Psi_2 + \Sigma\Phi}{\frac{4}{3}\pi r_{gr0}^3} = \left(Y\dot{f}t - c_g - c_b n_b\right) \cdot (1 - v_r) + \frac{3N_{bx}C_{bx}v_r}{2r_{grx}} \qquad (8)$$

The Inner Pressure of the Gas Bubbles

When the UMo grains are fully recrystallized, the gas bubbles would be almost in a uniform distribution. With the assumption that the gas bubbles are all spherical, the bubble volume fraction of *poro* meets

$$poro = \frac{\Delta V_{gas}}{V_0 + \Delta V_{gas} + \Delta V_{solid}} = \frac{SW_{gas}}{1 + SW_{gas} + SW_{solid}} \qquad (9)$$

where V_0 is the origin volume of a local part of fuel meat. ΔV_{gas} and ΔV_{solid} represent the volume increments caused by the fission gas and fission solid products; SW_{gas} and SW_{solid} respectively represent the induced gas swelling and solid swelling, with the total swelling $SW = SW_{gas} + SW_{solid}$.

Considering the volume change only results from the irradiation swelling, we have

$$\frac{V_e - V_0}{V_0} = SW \qquad (10)$$

where V_e represents the volume of the unit cell under the current configuration, and the original volume V_0 can be correlated as

$$V_0 = \frac{V_e}{1 + SW} \qquad (11)$$

The number of the gas atoms in the equivalent gas bubbles is:

$$N_\Sigma = \frac{n_\Sigma V_e}{1 + SW} \qquad (12)$$

It should be mentioned that when the gas bubbles are large enough, the influence of the surface tension in the bubbles could be ignored. In the unit cell, the gas atoms in the bubbles satisfy the Van der Waals gas-state equation, expressed as

$$p_{in}\left(V_g - h_s b_v N_\Sigma\right) = N_\Sigma kT \qquad (13)$$

where p_{in} in Pa is the equivalent inner pressure of the gas bubbles; $V_g = V_e \times poro$ is the volume of the gas bubbles; k is the Boltzmann's constant; and T is temperature in K; h_s is 0.6 in this research, and b_v is the Van der Waals gas constant in 8.5×10^{-29} m³/atom.
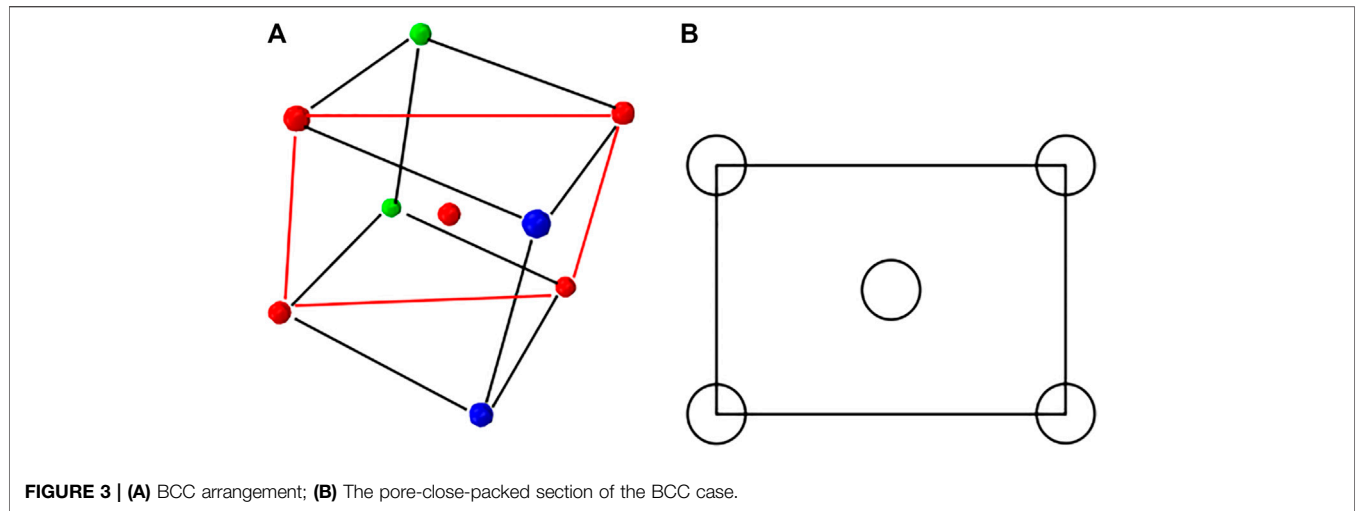
Combining **Eqs 12, 13** yields:

$$p_{in} \times \left(V_e \times poro - h_s b_v n_\Sigma \frac{V_e}{1 + SW}\right) = \frac{V_e}{1 + SW}n_\Sigma kT \qquad (14)$$
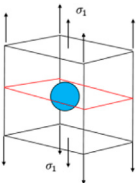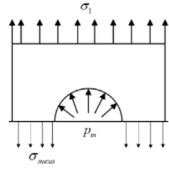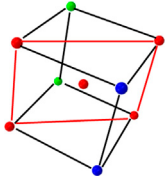
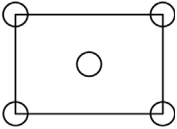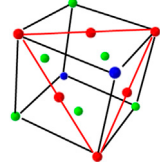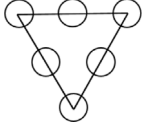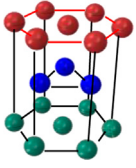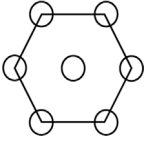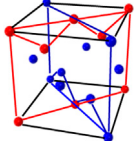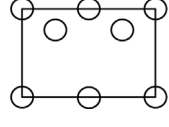Finally, the equivalent inner pressure is described as:

$$p_{in} = \frac{n_\Sigma kT}{poro\left(1 + SW\right) - h_s b_v n_\Sigma} = \frac{n_\Sigma kT}{SW_{gas} - h_s b_v n_\Sigma} \qquad (15)$$

When only considering the influence of the intergranular gas bubbles, the inner pressure can be described as:

FIGURE 3 | (A) BCC arrangement; (B) The pore-close-packed section of the BCC case.

TABLE 1 | x_p in different bubble distribution patterns.

Arrangement	Geometry model	Close-packed section	The maximum packing rate (%)	x_p
SC			52.36	1.209
BCC			68	1.077
FCC			74	1.108
HCP(hexagonal close-packed structure)			74	1.108
Diamond			34	0.855

$$p_{in2} = \frac{n_{\Sigma2}kT}{poro(1+SW)-h_sb_vn_{\Sigma2}} = \frac{n_{\Sigma2}kT}{SW_{gas}-h_sb_vn_{\Sigma2}} \quad (16)$$

Maximum Skeleton Stress of the Porous UMo Fuel Meat

The UMo alloy presents brittle failure after irradiation (Schulthess et al., 2019). For the further research on the brittle failure mechanism of the fuel meat, the maximum tensile stress on the mesoscale should be studied. To consider the influences of the porosity and pore pressure on the maximum skeleton stress, this study assumes that the macroscale first principle stress is along the normal direction of the pore-close-packed section, which is the most dangerous section to initiate cracking. Thus, the largest tensile stress in the fuel skeleton can be obtained. In Refs. (Jian et al., 2019a)' (Yan et al., 2019b), the skeleton stresses of FCC (Face Centered Cubic) and SC (Simple Cubic) bubble distribution pattern were respectively presented. However, the chosen section of FCC case was not the pore-close-packed section. In this study, the maximum skeleton stress model will be further developed.

The study of maximum skeleton stress will start from some certain distribution patterns. As shown in **Figure 3**, the close-packed section of the BCC (Body Centered Cubic) case is the red plane across the center of the gas bubbles.

It should be mentioned that the fission-gas swelling contributed by the intergranular gas-bubbles is much larger than the intragranular gas-bubble (Zhao et al., 2016). In this research, the inner pressure of the intergranular gas-bubbles is used in the calculation of the maximum skeleton stress. According to the static equilibrium equation, given as

$$\sigma_1\sqrt{2}a^2 + p_{in2}2\pi r^2 = \sigma_{meso}(\sqrt{2}a^2 - 2\pi r^2) \quad (17)$$

one can obtain

$$\sigma_{meso} = \frac{\sigma_1 + \sqrt{2}p_{in2}\pi\left(\frac{r}{a}\right)^2}{1 - \sqrt{2}\pi\left(\frac{r}{a}\right)^2} \quad (18)$$

In the above equations, σ_{meso} is the equivalent tensile stress of the fuel meat on the pore-close-packed section, which represents the maximum skeleton stress. σ_1 is the macroscale first principle stress.

For the BCC case, the pore radius r and edge-length a meet

$$\frac{2\times\frac{4}{3}\pi r^3}{a^3} = poro \quad (19)$$

Combining **Eqs 18**, **19**, the maximum skeleton stress of the fuel meat could be obtained as

$$\sigma_{meso} = \frac{\sigma_1 + 1.077\,poro^{\frac{2}{3}}\cdot p_{in2}}{1 - 1.077\,poro^{\frac{2}{3}}} \quad (20)$$

For some other bubble-distribution patterns, the maximum skeleton-stress models can be similarly derived out, and they could be expressed in a unified form:

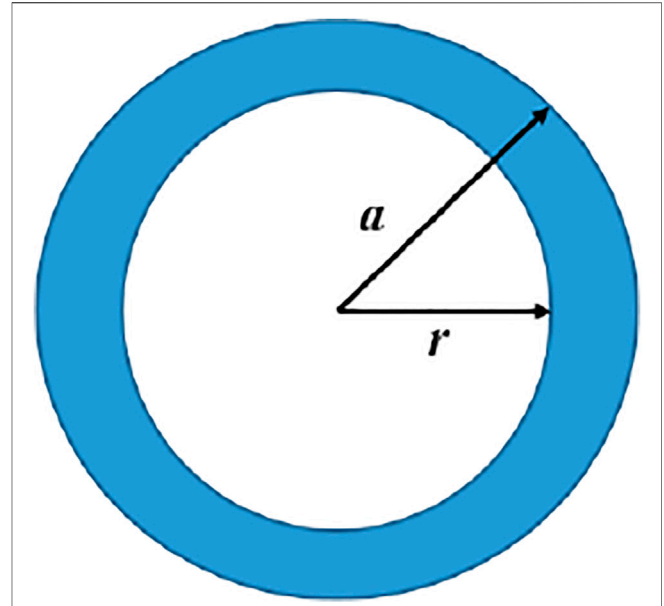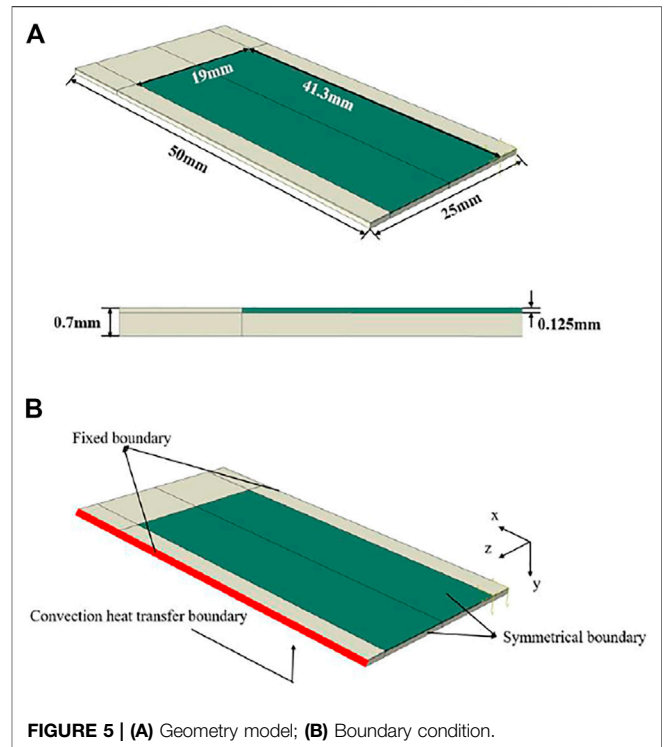**FIGURE 4 |** The RVE for the random distribution pattern.

FIGURE 5 | (A) Geometry model; **(B)** Boundary condition.

$$\sigma_{meso} = \frac{\sigma_1 + p_{in2}\cdot poro^{\frac{2}{3}}\cdot x_p}{1 - poro^{\frac{2}{3}}\cdot x_p} \quad (21)$$

where x_p is a parameter related to the distribution patterns of the gas bubbles, as given in **Table 1**. It should be mentioned that the

Maximum element length(mm)	Minimum element length(mm)	Nodes	Elements
0.5	0.1	300532	261306

maximum packing rate for most of the distribution patterns are very large, which implies that the porosity needs to be high enough to initiate cracking if the skeleton stress and strength are not considered. However, the post-irradiation examinations indicated that the cracking occurs at the porosity of ~30%. Thus, the prediction of the fuel failure should allow for the evolution of the skeleton stresses.

According to **Eq. 21**, the maximum skeleton stress of the fuel meat will be higher with a larger value of x_p. For a common arrangement mode, the expression of x_p could be developed.

On the assumption that a certain arrangement of the pores meets the conditions below:

1) There are n_{pore} pores in the representative cube;
2) The relative value of the area of the weak section in the cube cross section is S;
3) The number of the pores on the weak section is m.

On the weak section, the static equilibrium equation is shown as below:

$$\sigma_1 Sa^2 + p_{in2} \cdot m\pi r^2 = \sigma_{meso}\left(Sa^2 - m\pi r^2\right) \qquad (22)$$

The maximum skeleton tensile stress is:

$$\sigma_{meso} = \frac{\sigma_1 + p_{in2}\frac{m\pi r^2}{Sa^2}}{1 - \frac{m\pi r^2}{Sa^2}} \qquad (23)$$

According to **Eq. 21**, there is:

$$poro^{\frac{2}{3}} \cdot x_p = \frac{m\pi r^2}{Sa^2} \qquad (24)$$

The relationship among porosity, the radius of the pores r, the numbers of the pores n_{pore} and the edge-length of the representative cube a meets:

$$poro = \frac{n_{pore} \cdot \frac{4}{3}\pi r^3}{a^3} \qquad (25)$$

Finally there is:

$$x_p = \frac{m\pi^{1/3}}{S\left(\frac{4}{3}n_{pore}\right)^{2/3}} \qquad (26)$$

The gas pores are randomly distributed in the fuel meat (Gan et al., 2012; Kim et al., 2013a). For a completely random and uniform distribution pattern, the bubble distribution can be regarded as isotropy. The representative volume element can be established as an equivalent sphere containing a spherical bubble (Wei et al., 2019), as shown in **Figure 4**. The radius of the gas bubble is r, and the radius of the fuel element is a.

The porosity of the RVE is:

$$poro = \frac{r^3}{a^3} \qquad (27)$$

The mesoscale skeleton stress can be described as:

$$\sigma_{meso} = \frac{\sigma_1 + p_{in2}\left(\frac{r}{a}\right)^2}{1 - \left(\frac{r}{a}\right)^2} = \frac{\sigma_1 + p_{in2}\,poro^{2/3}}{1 - poro^{2/3}} \qquad (28)$$

which represents that x_p in this case is 1.

The gas bubble distributions still have uncertainties, so it is necessary to investigate the effects of bubble distribution patterns.

It is noted that the developed models in this section are suitable for the high burn-up cases.

FINITE ELEMENT MODEL

A finite element model is built to simulate the macro-mesoscale in-pile thermal-mechanical behaviors of the U-10Mo/Zr monolithic fuel plate. According to a certain irradiation condition in RERTR-9 (Kim et al., 2013b), the fission rate of the fuel meat is set as (Kong et al., 2018):

$$\dot{f} = \dot{f}_0 \cdot \beta \qquad (29)$$
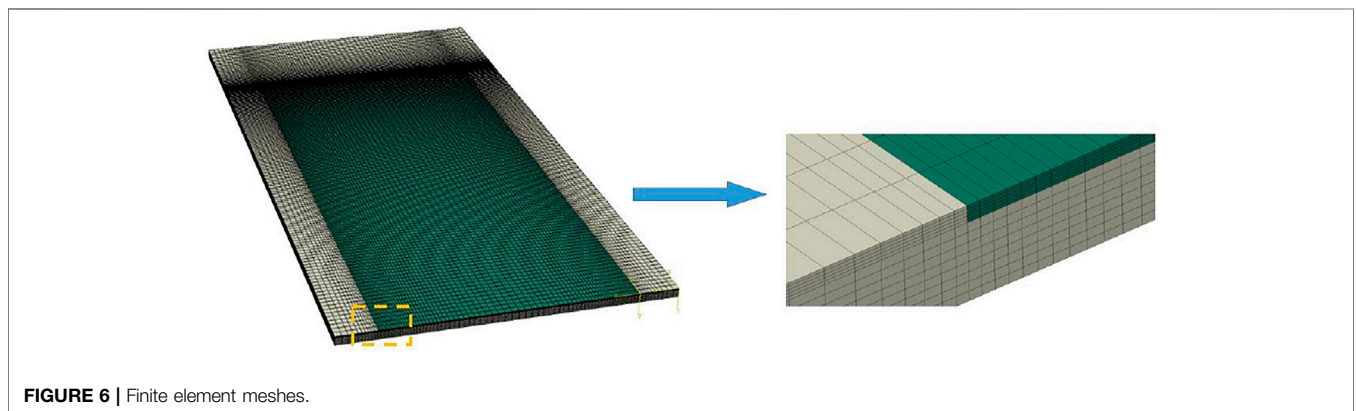
FIGURE 6 | Finite element meshes.

FIGURE 7 | **(A)** The distribution of the thickness displacement of the fuel meat after the 120 days irradiation; **(B)** the evolution of the thickness along Path 1.

FIGURE 8 | **(A)** The distribution of the thickness displacement of the fuel meat under 120 days irradiation; **(B)** post irradiation shape of UMo/Al fuel plate (Kim and Hofman, 2011).
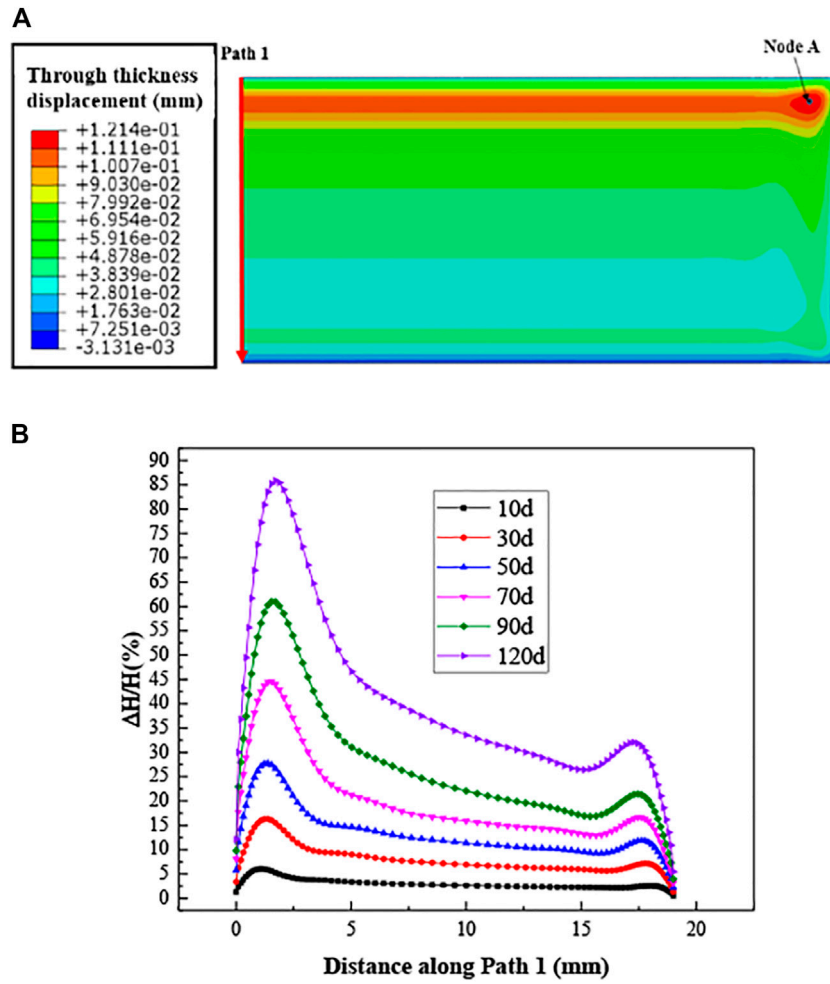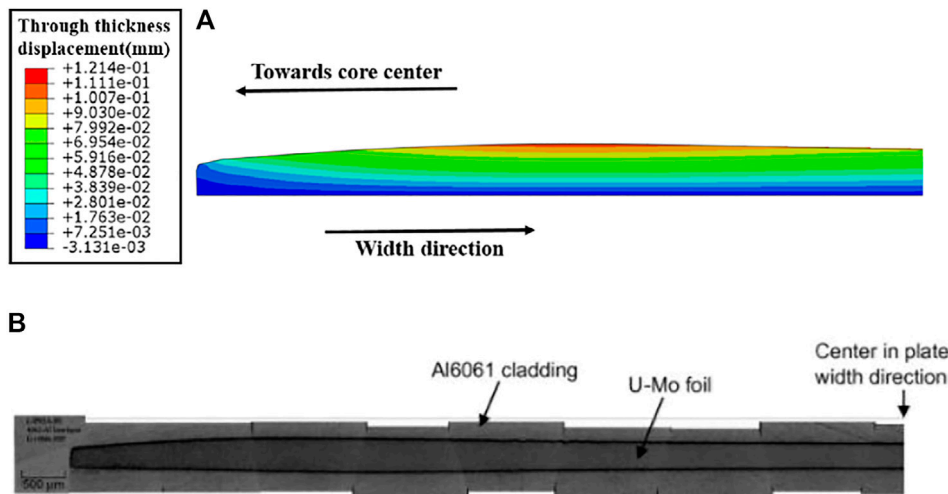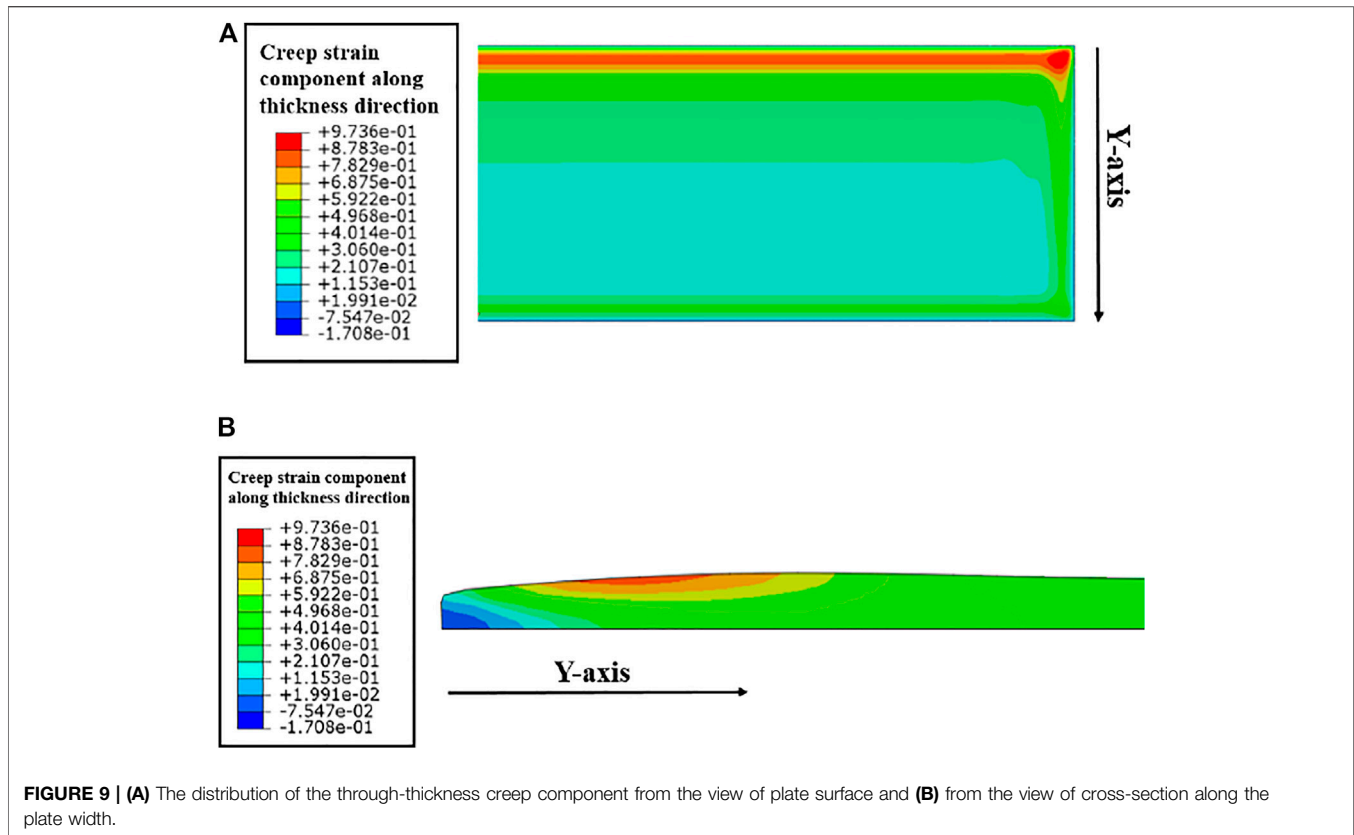
FIGURE 9 | (A) The distribution of the through-thickness creep component from the view of plate surface and **(B)** from the view of cross-section along the plate width.

$$\beta = 3.567 \times 10^{-5} y^4 - 1.672 \times 10^{-3} y^3 + 3.026 \times 10^{-2} y^2 - 0.2752 y$$
$$+ 1.900$$

$$(30)$$

where β is the distribution function of the fission rate. y means the distance along the width direction to the edge with the strongest irradiation. $\dot{f}_0$ is the average fission rate, and has a value of 6.0×10^{20} fission/m³s.

The fuel meat is considered to be well bonded with the cladding. The geometrical dimension of the plate is $100.0 \times 25.0 \times 1.4$mm, while that of the fuel meat is $82.6 \times 19.0 \times 0.25$mm (Kong et al., 2018). According to the symmetries in the plate shape and load, the finite element model is chosen as a 1/4 of the whole plate to reduce the computational scale. The thermal-mechanical properties of the fuel meat and cladding are introduced by the corresponding user-defined subroutines, which could be found in the related studies (Zhao et al., 2015; Kong et al., 2018). For the fuel meat, the irradiation swelling and irradiation creep are taken into consideration. The irradiation swelling strain is coupled with the fission rate, the temperature and local external hydrostatic stress (Kong et al., 2018). For the zircaloy cladding the irradiation hardening, the irradiation creep and irradiation growth are introduced. The detailed models and algorithms can be found in Ref. (Gong et al., 2014; Zhao et al., 2015). The thermal-mechanical boundary conditions are shown in **Figure 5**. The element of C3D8RT, a 3-D, 8-node, trilinear, coupled displacement-temperature, with a reduced integration element type, is used. The mesh grid parameters are listed in **Table 2**, with the details depicted in **Figure 6**.

As shown in **Figure 5B**, there is a thermal boundary condition set on the lower surface (the x-z plane), which satisfies $-k(\frac{\partial T}{\partial n}) = h(T - T_f)$, with the coolant temperature $T_f = 323$K, the heat exchange coefficient $h = 0.035$W/mm²K, $\frac{\partial T}{\partial n}$ means the temperature gradient component along the normal direction of the surface.

The other surfaces meet the adiabatic boundary condition, which is $-k(\frac{\partial T}{\partial n}) = 0$.

RESULTS AND DISCUSSION

The Macro-Deformation Fields
The Thickness Increments of the Fuel Meat

As shown in **Figure 7**, the thickness of the fuel meat increases faster at the side with stronger irradiation and suffering the highest temperature. With increasing the burn-up, the thickness of the fuel meat grows, and finally forms the shape similar as the results of UMo/Al fuel plate in **Figure 8B**. On the 30th day, the maximum thickness increases by 16.3%, and the average thickness increment per day is 0.543%. From the 30th day to the 90th day, the maximum thickness relative increment reaches 61.02%, and the average thickness increment per day is 0.745%. From the 90th day to the 120th day, the above two value are respectively 85.87 and

FIGURE 10 | (A) The distribution of the thickness displacement of the fuel meat after the 120-days irradiation; **(B)** Evolution of the total irradiation swelling strain and **(C)** the fission gas swelling strain along Path 1; **(D)** Distribution of each strain on the 120th day along Path 1.

FIGURE 11 | Temperature distribution of the fuel meat after 120 days irradiation.
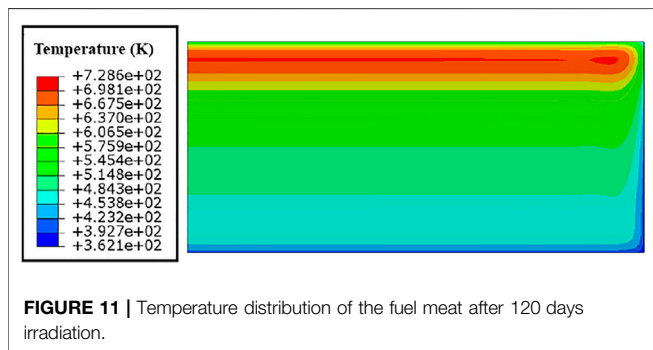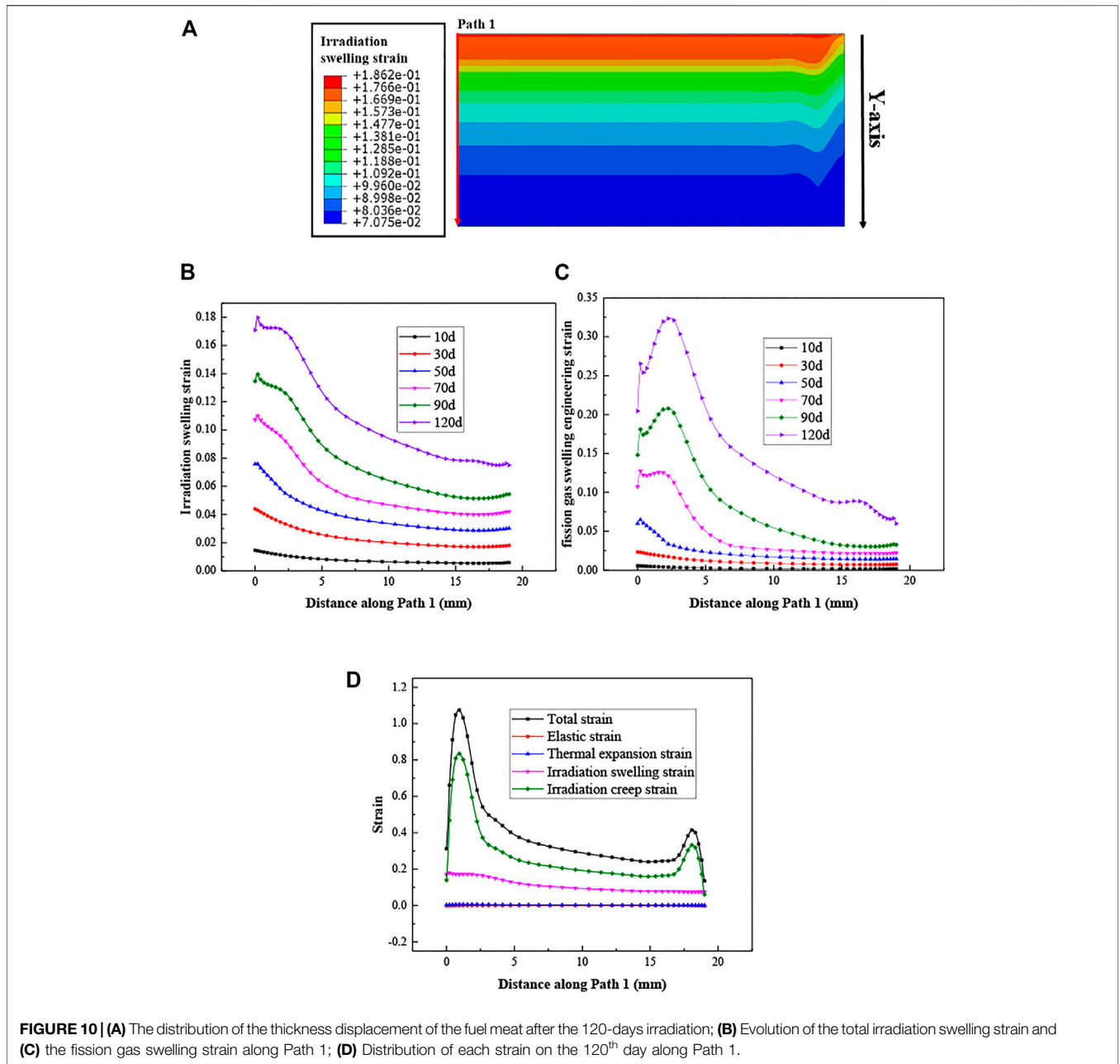
0.828%. The increase acceleration stems from the grain recrystallization.

The Contributions of Irradiation Swelling and Creep

The distribution of the through-thickness irradiation creep strain can be found in **Figure 9**. The maximum value occurs at the location near the corner with high irradiation. As shown in **Figure 9B**, with the influence of irradiation creep, the fuel meat at the edge region tends to flow towards the center, which affects the post-irradiation shape of the fuel meat.

Figure 10B displays the total irradiation swelling, which basically obeys the same distribution as the fission rate in the
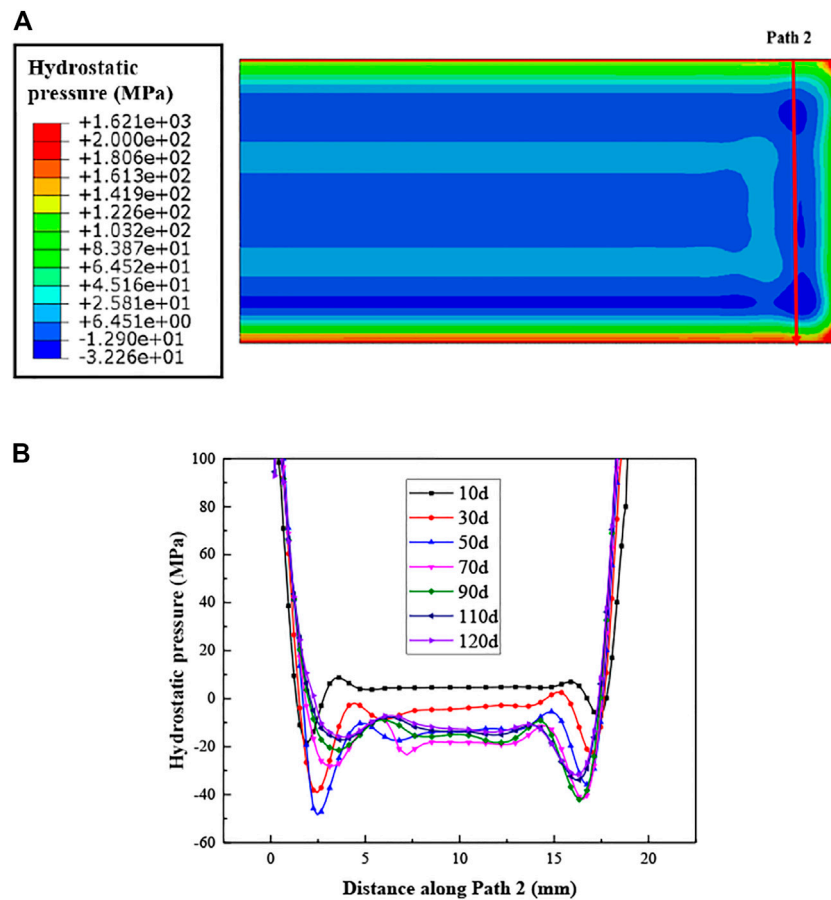
FIGURE 12 | (A) Distribution of the hydrostatic pressure (the upper side has a larger fission rate) and **(B)** evolution of the hydrostatic pressure along Path 2.

width direction, and is uniformly distributed along the length direction, except the small fluctuations near the ends. These fluctuations are attributed to the locally enhanced hydrostatic pressures near the ends, which result in the locally reduced fission gas swelling in **Figure 10C**. As shown in **Figure 10D**, the through-thickness strains of irradiation swelling and creep are the dominant contributions of the meat thickness increments. One can see that the irradiation creep strains are much larger than the swelling strains, and the irradiation creep strains determine the post-irradiation shape of the fuel meat. This appearance is consistent with that in Ref. (Jian et al., 2019b).
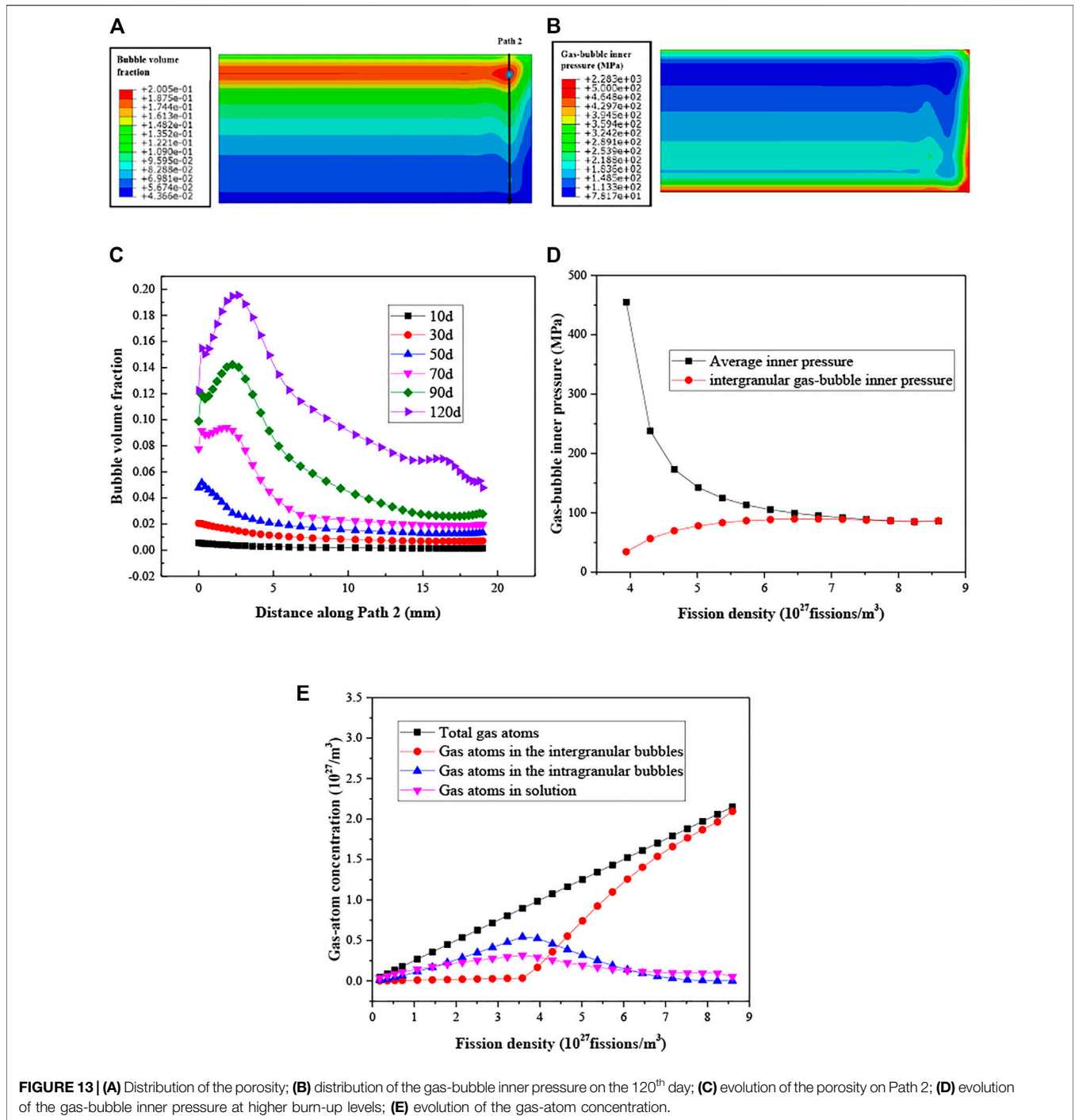
The fission gas swelling results in **Figure 10C** can be explained by the results of the hydrostatic pressures and temperature in **Figures 11**, **12**. After the 120 days irradiation, the hydrostatic pressures are much higher at the edge regions and near the corners, together with locally lowered temperature. There exists the regions with negative hydrostatic pressures, with the distances away from the ends ranged from 2-5 mm, which tend to give rise to the fission gas swelling. From the curves of fission gas swelling in **Figure 10C**, one can find that the values are the largest at

the location that is about 3 mm away from the heavily irradiated end.
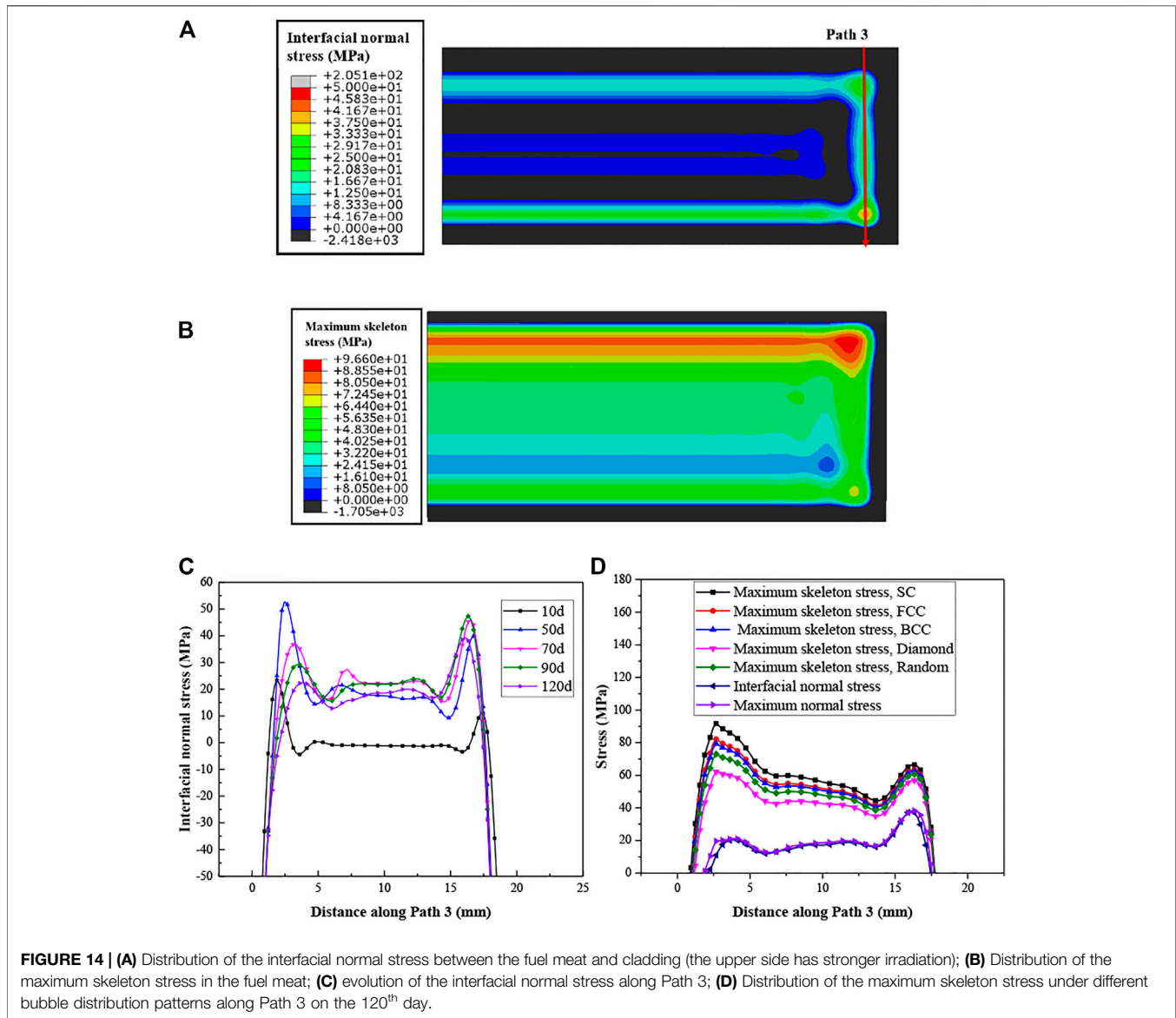
The Porosity and Gas-Bubble Inner Pressure

It could be observed from **Figure 13A** that the gas bubble volume fraction is larger near the side with the strongest irradiation. The porosity here could be up to 20% on the 120th day. As shown in **Figure 13C**, the porosity near the heavily irradiated end increases faster after the 30th day. It could be seen from **Eq. 9** that the porosity is mainly related to the fission gas swelling, thus the distribution and evolution of the porosity in **Figure 13** is similar to those of the fission gas swelling.

After the recrystallization begins, the evolution of the gas-bubble inner pressure for the blue point in **Figure 13A** is shown in **Figure 13D**. This phenomenon was also predicted in Ref. (Jian et al., 2019b). From the 55th day to the 120th day, the pressure decreases by 368.4 MPa. From **Figures 13A,B**, one can see that the gas-bubble inner pressure is extremely high at the corners and edges of the fuel meat, and the gas-bubble inner pressure is lower at the high-porosity area. As depicted in

FIGURE 13 | (A) Distribution of the porosity; **(B)** distribution of the gas-bubble inner pressure on the 120th day; **(C)** evolution of the porosity on Path 2; **(D)** evolution of the gas-bubble inner pressure at higher burn-up levels; **(E)** evolution of the gas-atom concentration.

other researches, when the recrystallization begins, the fission gas swelling rises more quickly (Cui et al., 2015; Robinson et al., 2021). However, the rate of the production of the fission gas atoms does not change (Cui et al., 2015), as shown in **Eq. 1**). Therefore, the gas atoms number in the bubbles keeps increasing linearly. The bubble inner pressure decreases to match the gas-state equation. The inner pressure of the intergranular bubbles rises with the increase of burn-up, because more gas atoms are released into the intergranular bubbles, as shown in **Figure 13E**. With the used irradiation-swelling model, most of the gas atoms are predicted to be in the intergranular bubbles, when the recrystallization process is finished. The values of p_{in} and p_{in2} are the same. At lower burnup levels, the average pressures are much higher than those of the intergranular-bubble inner pressures, which results from the contribution of the extremely high intragranular-bubble inner pressure (Hu et al., 2017).

FIGURE 14 | (A) Distribution of the interfacial normal stress between the fuel meat and cladding (the upper side has stronger irradiation); **(B)** Distribution of the maximum skeleton stress in the fuel meat; **(C)** evolution of the interfacial normal stress along Path 3; **(D)** Distribution of the maximum skeleton stress under different bubble distribution patterns along Path 3 on the 120th day.

Macro-Mesoscale Stress Fields

After the 120 days irradiation, the interfacial normal stress, which means the normal stress component on the interface between the fuel meat and cladding, is shown in **Figure 14**.

On the interface between the fuel meat and cladding, some areas experience tensile stresses. If the interface strength is weak there, separation could take place during irradiation. On Path 3, the peak tensile stress values locate near the heavily irradiated end, but not just at this end. The peak values rises firstly, and then falls. If the interface strength is high enough, the interface delamination will not occur, and the porous fuel meat is possible to be cracked, as mentioned in the part of Introduction. The cracking of the fuel meat depends on the maximum skeleton stresses.

It could be seen from **Figure 14B** that there are large values of the maximum skeleton stresses near the meat corner after the 120 days irradiation, which are much higher than the macroscale

first principal stresses. The distribution of the maximum skeleton stresses is similar to that of the interfacial normal stress and the first principle stress. However, at the center of the fuel meat/cladding interface, the interfacial normal stress is negative or near zero, while the maximum skeleton stress is up to ~60 MPa. The tensile skeleton stresses in the fuel meat may cause the cracking of the fuel meat. The macroscale first principal stresses of the fuel meat close to the interface are very similar to the interfacial normal stresses, which implies the corresponding section is vertical to the interface. If the fuel meat fails, the crack plane would be in parallel to the interface of the fuel meat and cladding. The maximum skeleton stress is almost 4–5 times of the macroscale first principal stress. Therefore, the failure prediction of the fuel meat should consider the effect of porosity and bubble inner pressure.

Simultaneously, one can observe from **Figure 14D** that the maximum skeleton stresses vary with the bubble distribution

patterns. When the gas bubbles obey the SC arrangement, the maximum skeleton stress has the largest value, while the diamond arrangement has the least. For the cases of the BCC and FCC arrangements, the peak values are nearly the same, which are a bit lower than that of the SC arrangement, and higher than the random-distribution case. Except for the diamond-pattern case, the peak stress values for the other cases locate near the heavily irradiated edge. The distribution of the maximum skeleton stress for the diamond-pattern case is more like the distribution of the first principle stress, because the influence of the gas-bubble inner pressure is less with smaller x_p. It can be concluded that the results of the SC arrangement can be used for the fuel failure, which are the most conservative.

CONCLUSION

In this study, the theoretical models for the porosity, the gas-bubble inner pressure and the maximum skeleton stress of the fuel meat were further developed, with the effects of the bubble distribution patterns considered. The macro-mesoscale thermal-mechanical behavior of the UMo/Zr monolithic fuel plate were obtained and analyzed, with the new models adopted. The main conclusions are summarized as:

1) The fission gas swelling and porosity of the fuel meat depends on the grain recrystallization process, and the greatly affected by the external hydrostatic pressures. The bubble inner pressure falls quickly after the grain recrystallization begins.
2) The maximum skeleton stresses of the fuel meat may reach ~4 times of the macroscale first principal stresses, which demonstrates that it is necessary to include the contributions of bubble fraction and pressure in the fuel failure predictions.
3) The arrangements of the gas bubbles in the fuel meat may have an distinct effect on the maximum skeleton stresses. These results of the SC arrangement are the most conservative for the predictions of the porous fuel meat.

In this research, the maximum skeleton stress is based on the assumption of uniformly distributed intergranular gas-bubbles. When the UMo alloy is not fully recrystallized, the intergranular gas-bubbles may not obey the uniform distribution. In the future works, a local porosity model is needed to be established for obtaining more reasonable mesoscale skeleton stresses. Besides, the thermal-mechanical properties of the UMo alloy such as the

elastic modulus, the thermal conductivity and the irradiation creep need to be correlated with the porosity. Combined with more experimental data of fission-gas related behavior, a multi-field coupling and multi-scale fracture model for the UMo monolithic fuel plate can be developed in the future, based on the mesoscale skeleton stress model, to predict the fuel fracture and analyze the fracture mechanism.

Indeed, the model for the skeleton stress is developed, based on the mechanistic fission gas-swelling model in the reference, so the precision of the maximum stress is dependent on the reasonability of the adopted gas-swelling model. The current fission gas-swelling model can capture the experimental results of the swelling, which should be further improved to match the experimental data about the bubble density and radius.

DATA AVAILABILITY STATEMENT

The raw data supporting the conclusion of this article will be made available by the authors, without undue reservation.

AUTHOR CONTRIBUTIONS

XK: Software, Validation, Formal analysis, Investigation, Data Curation, Writing—Original Draft, Visualization XJ: Software, Validation, Investigation, Data Curation, Writing—Original Draft FY: Software, Validation, Formal analysis, Investigation, SD: Conceptualization, Methodology, Software, Resources, Writing—Review & Editing, Supervision, Project administration WL, ZG, CL, YL: Conceptualization, Methodology, Resources, Supervision, Project administration All authors contributed to article revision, read, and approved the submitted version.

FUNDING

ACKNOWLEDGMENTS

REFERENCES

Booth, A. H. (1957). *Atomic Energy of Canada Limited Report[J]*AECL-496.

Burkes, D. E., Casella, A. M., Casella, A. J., Buck, E. C., Pool, K. N., MacFarlan, P. J., et al. (2015). Thermal Properties of U-Mo Alloys Irradiated to Moderate Burnup and Power. *J. Nucl. Mater.* 464, 331–341. doi:10.1016/j.jnucmat.2015.04.040

Cui, Y., Ding, S., Chen, Z., and Huo, Y. (2015). Modifications and Applications of the Mechanistic Gaseous Swelling Model for UMo Fuel. *J. Nucl. Mater.* 457 (Suppl. C), 157–164. doi:10.1016/j.jnucmat.2014.11.065

Gan, J., Keiser, D. D., Miller, B. D., Robinson, A. B., Jue, J. F., Medvedev, P., et al. (2012). TEM Characterization of U-7Mo/Al-2Si Dispersion Fuel Irradiated to Intermediate and High Fission Densities[J]. *J. Nucl. Mater.* 424 (1), 43–50. doi:10.1016/j.jnucmat.2012.02.001

Gan, J., Miller, B. D., Keiser, D. D., Jue, J. F., Madden, J. W., Robinson, A. B., et al. (2017). Irradiated Microstructure of U-10Mo Monolithic Fuel Plate at Very High Fission Density. *J. Nucl. Mater.* 492, 195–203. doi:10.1016/j.jnucmat.2017.05.035

Gong, X., Zhao, Y., and Ding, S. (2014). A New Method to Simulate the Micro-thermo-mechanical Behaviors Evolution in Dispersion Nuclear Fuel Elements. *Mech. Mater.* 77 (Suppl. C), 14–27. doi:10.1016/j.mechmat.2014.06.004

Gonzalez, A. G., Muñoz, C. A., and Arnaldo, G. J. (2015). Metallographic Study on Alloy Zircaloy-4 of Nuclear Use. *Proced. Mater. Sci.* 8, 494–501. doi:10.1016/j.mspro.2015.04.101

Holt, R. A., and Causey, A. R. (2004). Volume Conservation during Irradiation Growth of Zr-2.5Nb. *J. Nucl. Mater.* 335 (3), 529–533. doi:10.1016/j.jnucmat.2004.07.042

Hu, S., Setyawan, W., Joshi, V. V., and Lavender, C. A. (2017). Atomistic Simulations of Thermodynamic Properties of Xe Gas Bubbles in U10Mo Fuels. *J. Nucl. Mater.* 490, 49–58. doi:10.1016/j.jnucmat.2017.04.016

Jian, X., Kong, X., and Ding, S. (2019). A Mesoscale Stress Model for Irradiated U 10Mo Monolithic Fuels Based on Evolution of Volume Fraction/radius/internal Pressure of Bubbles. *Nucl. Eng. Tech.* 51 (6), 1575–1588. doi:10.1016/j.net.2019.04.011

Jian, X., Yan, F., Kong, X., and Ding, S. (2019). Effects of U-Mo Irradiation Creep Coefficient on the Mesoscale Mechanical Behavior in U-Mo/Al Monolithic Fuel Plates. *Nucl. Mater. Energ.* 21, 100706. doi:10.1016/j.nme.2019.100706

Jue, J.-F., Keiser, D. D., Miller, B. D., Madden, J. W., Robinson, A. B., and Rabin, B. H. (2018). Effects of Irradiation on the Interface between U-Mo and Zirconium Diffusion Barrier. *J. Nucl. Mater.* 499, 567–. doi:10.1016/j.jnucmat.2017.10.072

Kim, Y. S., Hofman, G. L., and Cheon, J. S. (2013). Recrystallization and Fission-Gas-Bubble Swelling of U–Mo Fuel[J]. *J. Nucl. Mater.* 436 (1), 14–22. doi:10.1016/j.jnucmat.2013.01.291

Kim, Y. S., Hofman, G. L., Cheon, J. S., Robinson, A. B., and Wachs, D. M. (2013). Fission Induced Swelling and Creep of U–Mo alloy Fuel[J]. *J. Nucl. Mater.* 437 (1), 37–46. doi:10.1016/j.jnucmat.2013.01.346

Kim, Y. S., and Hofman, G. L. (2011). Fission Product Induced Swelling of U–Mo alloy Fuel[J]. *J. Nucl. Mater.* 419 (1), 291–301. doi:10.1016/j.jnucmat.2011.08.018

Kong, X., Tian, X., Yan, F., Ding, S., Hu, S., and Burkes, D. E. (2018). Thermo-mechanical Behavior Simulation Coupled with the Hydrostatic-pressure-dependent Grain-Scale Fission Gas Swelling Calculation for a Monolithic UMo Fuel Plate under Heterogeneous Neutron Irradiation. *Open Eng.* 8 (1), 243–260. doi:10.1515/eng-2018-0029

Kong, X., Yang, H., and Ding, S. (2016). Zircaloy Plate Rolling Simulation with an Effective Strain-rate-dependent Stress-Updating Algorithm. *Int. J. Nonlinear Sci. Numer. Simulation* 17 (2), 113–125. doi:10.1515/ijnsns-2015-0077

Liu, M., and Chen, C. (2015). A Micromechanical Analysis of the Fracture Properties of Saturated Porous media. *Int. J. Sol. Structures* 63, 32–38. doi:10.1016/j.ijsolstr.2015.02.031

Liu, M., Zhang, Y., Wu, J., Gan, J., and Chen, C. Q. (2016). Analytical Solutions for Elastic Response of Coated Mesoporous Materials to Pore Pressure. *Int. J. Eng. Sci.* 107, 68–76. doi:10.1016/j.ijengsci.2016.07.010

Meyer, M. K., Gan, J., Jue, J. F., Keiser, D. D., Perez, E., Robinson, A., et al. (2014). Irradiation Performance of U-Mo Monolithic Fuel. *Nucl. Eng. Tech.* 46 (2), 169–182. doi:10.5516/net.07.2014.706

Miller, G. K., Burkes, D. E., and Wachs, D. M. (2010). Modeling thermal and Stress Behavior of the Fuel-Clad Interface in Monolithic Fuel Mini-Plates. *Mater. Des.* 31 (7), 3234–3243. doi:10.1016/j.matdes.2010.02.016

Miller, S. J., and Ozaltun, H. (2012). *Evaluation of U10Mo Fuel Plate Irradiation Behavior via Numerical and Experimental Benchmarking.* Asme International Mechanical Engineering Congress & Exposition. [C].

Pasqualini, E. E., Robinson, A. B., Porter, D. L., Wachs, D. M., and Finlay, M. R. (2016). Fabrication and Testing of U-7Mo Monolithic Plate Fuel with Zircaloy Cladding. *J. Nucl. Mater.* 479, 402–410. doi:10.1016/j.jnucmat.2016.07.034

Perez, D. M., Nielsen, J. W., Chang, G. S., and Ro, G. A. (2012). *AFIP-7 Irradiation Summary Report[R].* Idaho National Laboratory.

Perez, D. M., Lillo, M. A., Chang, G. S., Roth, G. A., Woolstenhulme, N. E., and Wachs, D. M. (2007). *RERTR-6 Irradiation Summary Report[J].*

Rest, J. (2005). A Model for the Effect of the Progression of Irradiation-Induced Recrystallization from Initiation to Completion on Swelling of UO 2 and U–10Mo Nuclear Fuels ☆[J]. *J. Nucl. Mater.* 346 (2), 226–232. doi:10.1016/j.jnucmat.2005.06.012

Rice, F. J. (2010). *U-mo Plate Blister Anneal Interim Report[R].*

Robinson, A. B., Williams, W. J., Hanson, W. A., Rabin, B. H., Lybeck, N. J., and Meyer, M. K. (2021). Swelling of U-Mo Monolithic Fuel: Developing a Predictive Swelling Correlation under Research Reactor Conditions. *J. Nucl. Mater.* 544, 152703. doi:10.1016/j.jnucmat.2020.152703

Rodriguez, P., Krishnan, R., and Sundaram, C. V. (1984). Radiation Effects in Nuclear Reactor Materials with Structure. *Bull. Mater. Sci.* 6 (2), 339–367. doi:10.1007/bf02743907

Rowcliffe, A. F., Mansur, L. K., Hoelzer, D. T., and Nanstad, R. K. (2009). Perspectives on Radiation Effects in Nickel-Base Alloys for Applications in Advanced Reactors. *J. Nucl. Mater.* 392 (2), 341–352. doi:10.1016/j.jnucmat.2009.03.023

Salvato, D., Leenaers, A., Van den Berghe, S., and Detavernier, C. (2018). Pore Pressure Estimation in Irradiated UMo. *J. Nucl. Mater.* 510, 472–483. doi:10.1016/j.jnucmat.2018.08.039

Schulthess, J. L., Lloyd, W. R., Rabin, B., Wheeler, K., and Walters, T. W. (2019). Mechanical Properties of Irradiated U Mo alloy Fuel. *J. Nucl. Mater.* 515, 91–106. doi:10.1016/j.jnucmat.2018.12.025

Snelgrove, J. L., Hofman, G. L., Meyer, M. K., Trybus, C. L., and Wiencek, T. C. (1997). Development of Very-High-Density Low-Enriched-Uranium Fuels. *Nucl. Eng. Des.* 178 (1), 119–126. doi:10.1016/s0029-5493(97)00217-3

Wei, H., Jian, X., and Ding, S. (2019). A Model of Gas-Induced Effective Expansion Strain for Porous Carbon Materials in Irradiation Environments. *J. Nucl. Mater.* 515, 338–353. doi:10.1016/j.jnucmat.2018.12.045

Yan, F., Kong, X., Ding, S., He, D. M., Li, Y. M., Chen, P., et al. (2019). Effects of Porous Fuel Structure on the Irradiation-Induced Thermo-Mechanical Coupling Behavior in Monolithic Fuel Plates[J]. *Scientia Sinica: Physica, Mechanica et Astronomica* 49 (11), 114606. doi:10.1360/sspma2018-00297

Yan, F., Jian, X., and Ding, S. (2019). Effects of UMo Irradiation Creep on the Thermo-Mechanical Behavior in Monolithic UMo/Al Fuel Plates. *J. Nucl. Mater.* 524, 209–217. doi:10.1016/j.jnucmat.2019.07.006

Zhao, Y., Gong, X., Cui, Y., and Ding, S. (2016). Simulation of the Fission-Induced Swelling and Creep in the CERCER Fuel Pellets. *Mater. Des.* 89, 183–195. doi:10.1016/j.matdes.2015.09.135

Zhao, Y., Gong, X., and Ding, S. (2015). Simulation of the Irradiation-Induced Thermo-Mechanical Behaviors Evolution in Monolithic U-Mo/Zr Fuel Plates under a Heterogeneous Irradiation Condition. *Nucl. Eng. Des.* 285, 84–97. doi:10.1016/j.nucengdes.2014.12.030